Modeling of Water Vapor Adsorption and Desorption in an Industrial Medical Air Dryer

Cristian Cardenas, David Farrusseng, Cécile Daniel

Modelling of water vapor adsorption and desorption in an industrial medical air dryer

Cristian Cardenas*, David Farrusseng, and Cécile Daniel

Université de Lyon 1, Institut de recherches sur la catalyse et l'environnement, 2 Avenue Albert Einstein, 69626 Villeurbanne, France.

*Corresponding author: cristian.cardenas@ircelyon.univ-lyon1.fr

Abstract

This study presents the development of a dynamic multiscale model to simulate the adsorption and desorption processes in a fixed bed for medical air drying. The model includes equations of mass balance, thermodynamics, hydrodynamics, and adsorption/desorption kinetics. The temperature-dependent Toth-Aranovich-Donohue equation is used to approximate the equilibrium relationship between water vapor and activated alumina/hopcalite. Measurements of the breakthrough curve at different water vapor concentrations and gas flow rates can be used to determine kinetic resistances such as axial dispersion, external film mass transfer, pore diffusion, and internal mass transfer, and thus to determine the limiting resistance of the process. The model predictions agree well with the experimental results, which are supported by performance indices and confirmed by additional breakthrough curves for validation. The validated model proves effective in predicting water vapor adsorption and desorption breakthrough curves on adsorbents considering concentration, flow rate, and temperature, and serves as a valuable tool for the development and optimization of commercial PSA columns with multiple adsorption layers.

Keywords: Industrial air dryer, Breakthrough curves, Modeling and simulation, Multiscale model, Water vapor adsorption.

1. Introduction

The air treatment system is an essential component of medical air systems [1]: It provides drying and purification of the compressed air produced to supply healthcare facilities with medical air, in fulfillment of the international standard NF EN ISO 7396-1 [2]. The dew point of the air treatment system reaches a

minimum of -45°C, i.e. 67 ppm [2], which allows for high air quality. A medical compressed air dryer is manufactured by a membrane process [3] or by pressure swing adsorption (PSA) [4] at room temperature using water-selective adsorbents. The major production of dry medical air is ensured by air compressors and a column operating in PSA mode with a countercurrent regeneration mode. There are several materials that can be utilized for moisture adsorption, and their efficiency may vary depending on the specific application and conditions. Common moisture adsorbents comprise are molecular sieves, activated alumina, silica gel, activated carbon, and calcium chloride. Each material has unique properties, such as adsorption capacity, desorption methods. Silica gel is a highly porous material that can adsorb up to 40% of its weight in moisture and is easily desorbed by heating. Activated alumina, created by a chemical process that increases its surface area, can adsorb up to 20% of its weight in moisture, and is frequently utilized as a desiccant for moisture adsorption from gases and desorption requires heating. Molecular sieves, composed of aluminum silicates, have a highly organized pore structure that allows them to selectively adsorb moisture and are suitable for removing moisture from gases or liquids with extremely low dew points. They can adsorb up to 25% of their weight in moisture and can be desorbed by heating or depressurization. Calcium chloride, a solid that adsorbs moisture through chemical reactions, can absorb about 150% of its weight. Activated carbon, a porous material that can adsorb various impurities, including moisture, is efficient in adsorbing moisture from gases and liquids, it can adsorb about 5% of its weight in moisture and can be desorbed by heating or pressure reduction. It is essential to note that the efficiency of the adsorbent also depends on the relative humidity and temperature and pressure of the gas. Additionally, the cost and disposal of the spent adsorbent should be considered. Desorption is the process of removing adsorbed moisture from an adsorbent, with common desorption methods including heating, vacuum, and purging with dry inert gas. However, the required heating temperature and duration may vary depending on the material and amount of moisture adsorbed. It is important to note that desorption performance depends not only on the adsorbent, but also on the application and conditions, such as temperature, humidity, and pressure. In addition, the regeneration process of the adsorbent may weaken or damage the adsorbent, reducing its efficiency. The common industrial column is a fixed bed with several moisture adsorbents in the form of granules connected in series. The technology is based on the choice of the nature of the adsorbents, their

arrangement in the column and their respective volume. Qualitatively, adsorbents placed at the bottom of the column, where the moist air feed flow enters, are the least hydrophilic and adsorb the most moisture, while adsorbents placed at the top of the column are the most hydrophilic and allow moisture adsorption at low concentrations. The design of the industrial adsorption columns is based on the state of the art, i.e., most of the column packing consists of a combination of multi-adsorbents such as activated alumina [5] layer at the bottom of the column, an activated carbon [6] layer to treat the volatile organic compounds, and oil residues from pumps, a Mn-based metal oxide [7] (Hopcalite) layer to oxidize the carbon monoxide to carbon dioxide and is known also as a humidity adsorbent, and another layer of alumina at the top of the column to hold the different layers together, activated carbon does not significantly adsorb moisture in the system/process and is not considered in this work.

In the literature, Chout [8], Nastaj & Ambrożek [9], Ouchi et al [10], Ribeiro et al [11], Shi et al [12], proposed to analyze the dynamic adsorption of water vapor on alumina with a mathematical LDF model using the temperature-independent isothermal (BET and Langmuir) equations. The limitation of this model is that all the kinetic transfer resistances present in the process are lumped into a single coefficient and the prediction of the model at a different temperature is not guaranteed. Currently, there is no comprehensive study to model and simulate the dynamic process of adsorption and desorption of water vapor on several adsorbents at different operating conditions. Therefore, this study establishes a Fickian multiscale model that can accurately forecast the adsorption and desorption breakthrough curves on alumina and hopcalite in an industrial dryer, considering variations in gas flow rate, concentrations, and temperature. The uniqueness of our model lies in its ability to discern and separate various kinetic resistances, including external film mass transfer, pore diffusion, and internal mass transport coefficients. By doing so, we can determine the governing resistance that limits the overall process.

The dynamic behavior of a system is intricately affected by the interplay between the fluid and adsorbents, which is governed by the thermodynamic and kinetic properties of adsorption. The ability to forecast the behavior of an industrial air dryer without the aid of experimental measurements poses a significant challenge. To address this, a study was conducted to investigate the dynamic adsorption and desorption of water vapor using a reduced-scale column. This approach allowed for a better

understanding of the system's behavior on a smaller scale, providing valuable insights for industrial applications. This is possible because the time required for the fluid to pass through the column of the industrial air dryer is the same as in the reduced scale column. The methodology used is based on the characterization of adsorbents, the measurement of adsorption isotherms, the measurement of adsorption and desorption breakthrough curves and the development of a phenomenological model, its identification, validation, and implementation with experimental measurements. The result of this work is a statistically validated model that has the potential to greatly impact the design and optimization of industrial medical air dryers. By using this model, it is possible to predict the adsorption and desorption performances of different adsorbents under various operating conditions. This information can be used to optimize the process and improve the efficiency of the dryer. For example, the model can be used to evaluate the effect of different operating conditions, such as temperature, pressure, relative humidity, and adsorbent type and loading on the adsorption and desorption performance of the dryer. This can aid in identifying the optimal conditions for maximum adsorption and desorption efficiency and minimize energy consumption. Furthermore, the model can also be used to evaluate the cost and environmental impact of different adsorbent materials and regeneration strategies, which can aid in reducing the cost and increasing the sustainability of the dryer.

2. Experimental measurements

2.1. Characterization of the adsorbents

The commercial adsorbents studied were obtained from MILS, a French company specialized in drying compressed air. Hopcalite is in the form of irregular grains with an approximate diameter of 1.5 mm, while alumina is present as spherical particles with a diameter of about 2 mm. The porous structure of both adsorbents was characterized by manometry, using a liquid nitrogen isotherm at 77 K on a BelsorpMax instrument. Specific surface area was determined by the BET method [13] and pore size was estimated by the NLDFT method [14], both using Belmaster software (see Figures *S1* and *S2* in the Supporting Information). The true density of the solid was determined by helium pycnometry using the same instrument. All gasses used in the experiments, namely N_2 and He, were supplied by Air Liquide France with purity above 99.999%. The results of these measurements are shown in Table *1*.

Table 1: Characterization of adsorbents

	Alumina	***Hopcalite***
Specific surface area ($m^2.g^{-1}$)	329	309
Total pore volume, ($cm^3.g^{-1}$)	0.43	0.42
Mean pore diameter, (nm)	3.87	4.55
True density, ($kg.m^{-3}$)	2226	3282

2.2. Measurements of the adsorption equilibrium isotherms

Water vapor adsorption isotherms on activated alumina and hopcalite samples were determined using a BelsorpMax 2 instrument (Microtrac Bel) in the temperature range 293-313 K. The adsorption temperature was carefully controlled with a thermostatic bath (Dyneo DD -300F) with an uncertainty of ±0.1 K. To prepare the samples for adsorption measurements, a desorption step was performed under a primary vacuum in a Belprep vacuum ramp at 150°C for a period of 12 hours.

2.3. Dynamic adsorption measurements

To measure the adsorption and desorption breakthrough curves of water vapor, an experimental setup was used, which is shown in Figure *1*. Its main element is a reduced column filled with commercial adsorbent particles. The scaled-down column corresponds to the column of an industrial air dryer in that it contains the same adsorbents and operates under the same operating conditions. This is possible because in both columns the time required for the fluid to pass through the column is the same. In this way, a gas flow of 135 $mL.min^{-1}$ can be obtained, which corresponds to the average reference value of the feed gas flow in an industrial compressed air dryer, i.e. 117 $m^3.h^{-1}$ (for details, see section *S1* of the supporting information). The gas flow passes through a 40 mm length adsorbent packed in a glass tube with an inner diameter of 4 mm. The characteristics of the reduced column and the operating conditions are listed in Table *2*. Although the particle diameter to column diameter ratio ($\delta = D_c/d_{pe}$) is relatively low, which may lead to preferential flow paths and non-uniform flow, it is worth noting that this column diameter is not uncommon in the literature and has been used in previous studies [15,16]. In addition, we are aware of the potential for preferential flow paths in our study and have attempted to address this issue by careful packing of the adsorbent bed and a relatively low flow rate. In addition, a recent study by Petrazzuoli et al [17] showed that preferential pathways through the wall can occur when the value of

δ (column to sphere diameter ratio) is less than 1.78, whereas in our study the value of δ is between 2 and 2.7. This shows that despite the possibility of the formation of rings or holes in the center of the column, a uniform flow can be achieved. In summary, although the column diameter used in our study does not meet the best practices of Chem Eng, we are confident that the hydrodynamics of the column are sufficient for an experimental study and the research objectives based on the latest scientific studies.

Table 2: Adsorbent bed column characteristics and operating conditions.

Packed bed column	Diameter (mm)	Length (mm)	Bed porosity ($m_{gas}^3.m_{col}^{-3}$)	Particle porosity ($m_{gas}^3.m_{pe}^{-3}$)	Adsorbent mass (mg)	Bed density ($kg.m^{-3}$)	Relative humidity (%)
Value	4	40	0.5	0.47	370	753	15 to 80

The breakthrough curves were measured at a room temperature of 20 °C under dry and humid conditions. To create different humid conditions, the humid feed and dilution feed gas streams were mixed. The adsorbent particles are used without pretreatment. Pressure sensors are strategically positioned both upstream and downstream of the adsorbent bed column to monitor pressure differences. In addition, a Michell hygrometer moisture analysis sensor is used to measure partial pressure at the outlet of the column. The dry gas stream is used to maintain the material in a dry state or to facilitate its desorption. To facilitate data acquisition, all sensors are connected to a home-built acquisition module.

Experimental procedure

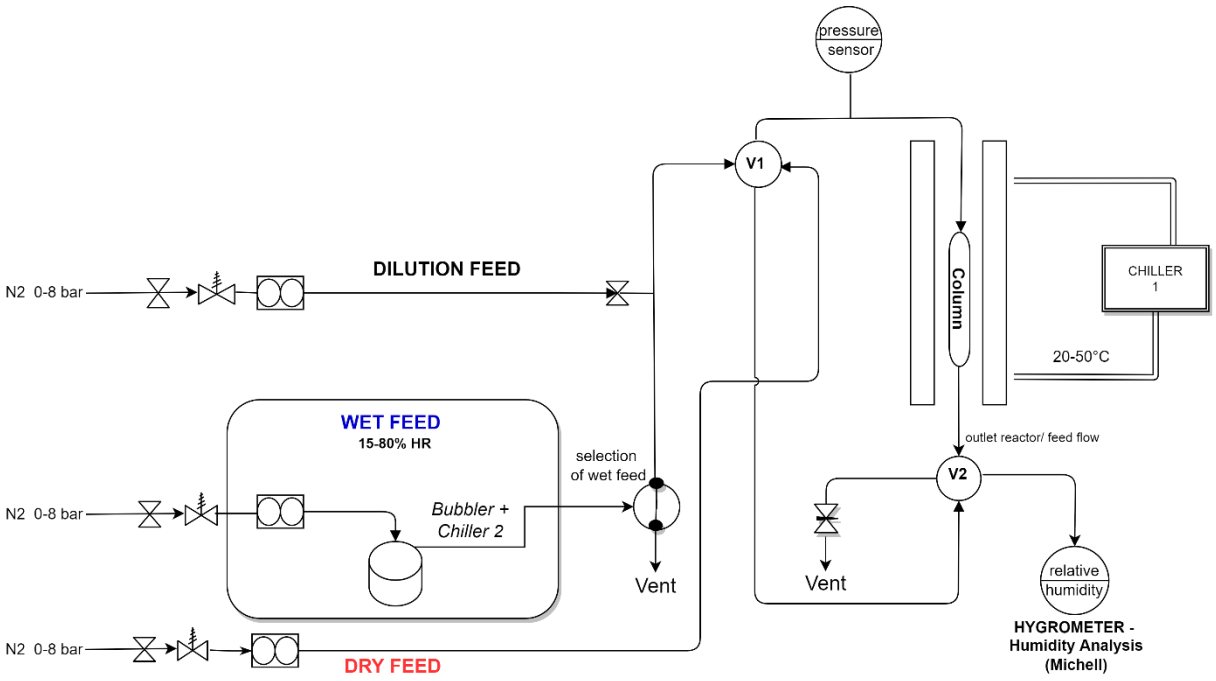

Figure 1: Experimental setup used for breakthrough curves measurements

Experimental procedure

The column is filled with approximately 370 mg of adsorbent particles. The temperature was monitored and controlled during the experiments using a water bath. Cooler 1 is set at 20 °C to ensure a constant temperature in the bed column. The choice of 20 °C as the measurement temperature for the breakthrough curves could be based on some factors. 20 °C is considered a standard temperature for many types of experiments and is within the range of typical room temperatures. This allows easy reproducibility of results and comparisons with other studies. The adsorbent bed column is kept under dry flow until the column stabilizes. To create the desired relative humidity, a gas stream is generated and supplied to the adsorption column. After reaching saturation, a dry gas stream is introduced to desorb and regenerate the column. To ensure thorough removal of moisture from the adsorbent, the desorption time is at least four times longer than the adsorption time. The experiments are conducted in triplicate to verify the repeatability and reproducibility of the results.

3. Model development

Adsorption isotherm and kinetic models are required to describe the water vapor adsorption process on selective water adsorbents. Therefore, an important step is to select the adsorption isotherm equation that best describes the thermodynamic equilibrium. This isothermal model shall predict the amount of equilibrium vapor that will be adsorbed at a given water concentration. As temperature rises, it is well-established that the adsorption capacity tends to decrease. Consequently, to provide a comprehensive understanding of the adsorption behavior of water vapor on adsorbents, it becomes necessary to employ a temperature-dependent model for the adsorption isotherm.

3.1. Adsorption equilibrium

The Toth-Aranovich-Donohue temperature-dependent equation is applied to accurately describe the water adsorption isotherms on alumina and hopcalite, which exhibit a type II isotherm, a characteristic of physical adsorption mainly on meso- and macropores [18]. This equation is well-suited for modeling adsorption on these types of pores, and accounts for the temperature dependence of the adsorption

process, providing a more precise representation of the adsorption behavior of these adsorbents. The equation used in this study to describe the equilibrium water vapor adsorption, represented by q_e (mol.kg^{-1}), as a function of water vapor concentration, c (mol.m^{-3}), is a semi-empirical equation comprising two terms. The first term corresponds to the Toth equation, which is suitable for describing heterogeneous adsorption systems and monolayer adsorption at low concentrations. This term accounts for the interactions between the adsorbate molecules and the adsorbent surface, incorporating a dimensionless heterogeneity factor, t_o. The second term represents the Aranovich-Donohue equation, specifically the type III isotherm, and includes an adjustable dimensionless factor, n_2. It is a modified form of the BET equation describing multilayer adsorption at high concentrations. The Toth-Aranovich-Donohue equation is expressed as follows [18]:

$$q_e = \left\{ \frac{q_m b c}{\left[1+(bc)^{t_o}\right]^{\frac{1}{t_o}}} \right\} \left[\frac{1}{(1-b_2 c)^{n_2}} \right] \tag{1}$$

with q_m (mol.kg^{-1}) the maximum adsorbed quantity which is temperature dependent as:

$$q_m = q_{m0} \exp\left[\chi \left(1 - \frac{T}{T_0} \right) \right] \tag{2}$$

b (m^3.mol^{-1}) the equilibrium constant at low concentrations which is temperature dependent as:

$$b = b_0 \exp\left[\frac{Q}{R_g T_0} \left(\frac{T_0}{T} - 1 \right) \right] \tag{3}$$

b_2 (m^3.mol^{-1}) the equilibrium constant at high concentrations which is temperature dependent as:

$$b_2 = b_{20} \exp\left[\frac{Q_2}{R_g T_0} \left(\frac{T_0}{T} - 1 \right) \right] \tag{4}$$

and t_o the Toth heterogeneity factor which is temperature dependent as:

$$t_o = t_{o0} + \alpha \left(1 - \frac{T_0}{T} \right) \tag{5}$$

The constants α, χ, and n_2 are utilized in the equation. The parameters q_{m0} (mol.kg^{-1}), b_0 (m^3.mol^{-1}), b_{20} (m^3.mol^{-1}), and t_{o0} represent the maximum adsorbed amount, the equilibrium constants at low and high

concentrations, and the Toth's heterogeneity factor at the reference temperature T_0 (K), respectively. Q and Q_2 (J.mol^{-1}) denote the heats of adsorption at the monolayer and multilayer levels. R_g (J.mol^{-1}.K^{-1}) represents the ideal gas constant. The optimal values of the Toth-Aranovich-Donohue isotherm equation (Eq.1) with nine unknown parameters, namely q_{m0}, b_0, b_{20}, t_{o0}, Q, Q_2, α, χ, and n_2, are presented in Table *3*, using a reference temperature of 298 K. The estimability and identification of the parameters of the Toth-Aranovich-Donohue model were discussed and presented in our previous work [18]. Some comments and isotherms of water vapor adsorption on alumina and hopcalite are given in Section *S4* of the Supporting Information.

Table 3: Identified parameter values of the Toth-Aranovich-Donohue equation.

	Parameters	q_{m0}	b_0	t_{o0}	Q/R_gT_0	α	χ	b_{20}	n_2	Q_2/RgT_0
Water vapor	*Value*	32.51	32.22	0.24	18.98	0.017	0.53	0.67	1.14	16.27
Alumina	*CI (95%)*	±1.64	±3.24	±0.01	±1.68	±0.01	±0.45	±0.01	±0.01	±0.16
Water vapor	*Value*	7.48	202.5	0.41	18.04	0.017	0.35	0.19	6.01	16.79
Hopcalite	*CI (95%)*	±0.90	±44.4	±0.05	±1.72	±0.01	±0.33	±0.02	±0.69	±0.43

3.2. Adsorption and desorption mechanism

The adsorption mechanism of water vapor on activated alumina or hopcalite is based on the process of physisorption. Physisorption is a weak interaction between the adsorbate molecules (water vapor) and the surface of the adsorbent (activated alumina/hopcalite). Activated alumina and hopcalite have a large surface area with numerous pores on their surface. The pores on the surface of the adsorbent are in the mesopore range, which is about 2-50 nm. When water vapor molecules encounter the surface of the adsorbent, they are adsorbed in these pores. The physisorption interaction is temperature dependent, and adsorption is stronger at low temperatures. The adsorption of water vapor on activated alumina or hopcalite occurs through the formation of hydrogen bonds between the adsorbate molecules and the surface of the adsorbent. The water vapor molecules are adsorbed in the pores, filling the voids, and forming a monolayer on the surface of the adsorbent. The desorption process of water vapor from activated alumina or hopcalite can be achieved through several methods, including heating, vacuum, or purging with dry inert gas. The desorption process is endothermic and requires energy input, and thus, the efficiency of desorption process is also affected by the temperature of the process. In summary, the

mechanism of adsorption and desorption of water vapor on activated alumina and hopcalite is based on physisorption, which occurs due to the formation of hydrogen bonds between the adsorbate molecules and the surface of the adsorbent and mainly takes place on the mesoporous structure of the adsorbent.

3.3. Dynamic adsorption process

A comprehensive one-dimensional multiscale model is developed to simulate the dynamic adsorption and desorption process of water vapor. The model is based on several assumptions: (i) the gas mixture follows the ideal gas law, (ii) water vapor is the sole adsorbed molecule, (iii) the pressure drop along the bed is accounted for using Ergun's equation, (iv) the resistance to mass transfer through the boundary layer surrounding the solid particles is represented by an external film mass transfer coefficient, (v) mass transfer within the particles is governed by Fick's diffusion and characterized by an effective diffusion coefficient in the macropores, (vi) mass transport of water vapor in the mesopores is attributed to mesopore diffusion, (vii) the equilibrium isotherm between the gas phase and the adsorbent is described by the Toth-Aranovich-Donohue equation, (viii) the adsorbent particles are assumed to be spherical and have homogeneous size, (ix) the temperature and physical properties of the adsorbent remain constant, (x) only the axial dimension is considered, leading to a one-dimensional model, (xi) the adsorption and desorption processes are reversible.

The multiscale model considers both the bed scale and the particle scale. At the particle scale, the model considers the presence of macro- and mesopores. A mass transfer coefficient is used to describe the mass transfer from the fluid phase in the bed column to the fluid phase at the particle surface. In addition, a pore diffusion coefficient is used to represent the transport of water vapor from the gas phase of the particle to the solid surface. The interaction between these two phenomena, convection and diffusion, is captured by the material Biot number. The equations of the water vapor mass balance for each scale can be expressed as follows:

(i) In the bed column, the equation for the water vapor mass balance in the gas phase is described as follows [19–21]:

$$\frac{\partial c}{\partial t} - D_{ax}\frac{\partial^2 c}{\partial z^2} + \frac{\partial (vc)}{\partial z} = -\frac{1-\varepsilon_b}{\varepsilon_b}\frac{3}{r_{pe}}k_f\left(c - c_{pe|r_p=r_{pe}}\right)\left(\frac{1}{1+B_i}\right) \quad (6)$$

The water vapor concentration in the gas phase is denoted as c (z,t) (mol.m^{-3}), where z represents the axial position within the bed column and t denotes time. The interstitial gas velocity is represented by $v=u/\varepsilon_b$ (m.s^{-1}), where u is the superficial gas velocity and ε_b is the bed porosity (m_{gas}^3.m_{col}^{-3}). The axial dispersion coefficient is defined as D_{ax} (m2.s-1). In addition, r_{pe} (m) represents the mean radius of the adsorbent particle, k_f (m.s^{-1}) is the external film mass transfer coefficient, and $c_{pe|r_p=r_{pe}}$ (mol.m^{-3}) corresponds to the water vapor concentration at the particle surface. The material Biot number, denoted B_i, quantifies the ratio of the mass transfer flux resulting from internal diffusion within the particle to the external mass transfer flux driven by convection in the particle film. When the material Biot number is greater than 3, the adsorption process is mainly driven by internal diffusive transport. On the other hand, if the material Biot number is less than 0.1, external mass transfer is the dominant mechanism. The material Biot number is determined as:

$$B_i = \frac{r_{pe}k_f}{5D_e} \quad (7)$$

The effective diffusion coefficient, denoted as D_e (m^2.s^{-1}), plays a crucial role in the model. It is influenced by the porosity ε_{pe} (m_{gas}^3.m_{pe}^{-3}), the tortuosity τ_{pe} (-), and the mixture diffusion D_M (m^2.s^{-1}) within the particle. In general, the effective diffusion coefficient can be expressed as follows:

$$D_e = \varepsilon_{pe}\frac{D_M}{\tau_{pe}} \quad (8)$$

(ii) In the particle, mass transport of water vapor occurs by Fickian diffusion, which is characterized by the effective diffusion coefficient. Assuming that there are no lateral and azimuthal variations in particle concentration, the water vapor mass balance in the radial direction is described as follows [22]:

$$\varepsilon_{pe}\frac{\partial c_{pe}}{\partial t} + \left(1-\varepsilon_{pe}\right)\frac{\partial q}{\partial t} = \frac{D_e}{r_p^{\,2}}\frac{\partial}{\partial r_p}\left(r_p^{\,2}\frac{\partial c_{pe}}{\partial r_p}\right) \quad (9)$$

The water vapor concentration in the gas phase is represented by c_{pe} (z, r_p, t) (mol.m^{-3}), while q (mol.m^{-3}) corresponds to the water vapor adsorbed on the particle in the solid phase. To describe the behavior

of water vapor in the mesopores, the linear driving force (LDF) model is used, which can be expressed as follows [23]:

$$\frac{\partial q}{\partial t} \approx \frac{\partial \bar{q}}{\partial t} = k_1\left(q_e^* - \bar{q}\right) \text{with } k_1 = \frac{15 D_{meso}}{r_{mp}^{\ 2}} \tag{10}$$

where $\bar{q}$ (mol.m^{-3}) represents the average adsorbed amount of water vapor on the solid surface, D_{meso} (m^2.s^{-1}) corresponds to mesopore diffusion, r_{mp} (m) denotes the average pore diameter, and $q_e^*=q_e \rho_s$ (mol.m^{-3}) represents the equilibrium adsorbed amount of water vapor considering the solid density. In addition, k_1 (s^{-1}) represents the internal linear driving force on the mesopores. To fully describe the phenomena, the equation is accompanied by the following initial and boundary conditions:

$$* t = 0 \qquad c = 0,\ c_{pe} = 0,\ \bar{q} = 0, \quad \forall z \text{ and } r_p \tag{11}$$

$$* z = 0 \qquad -D_{ax}\frac{\partial c}{\partial z} = v\left(c_0 - c\right),\ \forall t \text{ and } r_p \tag{12}$$

$$* z = L \qquad \frac{\partial c}{\partial z} = 0\ ,\ \forall t \text{ and } r_p \tag{13}$$

$$* r_p = 0 \qquad \frac{\partial c_{pe}}{\partial r_p} = 0,\ \forall z \text{ and } t \tag{14}$$

$$* r_p = r_{pe} \qquad -D_e\left(\frac{\partial c_{pe}}{\partial r_p}\right)_{r_p} = k_f\left(c - c_{pe|_{r_p = r_{pe}}}\right),\ \forall z \text{ and } t \tag{15}$$

The Ergun equation is used for the high gas flow during the fast charging process in industrial medical air. This equation considers not only viscous resistance, but also inertial resistance. The form of the Ergun equation is:

$$-\frac{\partial P}{\partial z} = a\mu_B u + b\rho_B u^2 \ \text{ with: } a = \frac{150}{d_{pe}^{\ 2}}\frac{(1-\varepsilon_b)^2}{\varepsilon_b^{\ 3}}, \quad b = 1.75\frac{(1-\varepsilon_b)}{d_{pe}\varepsilon_b^{\ 3}} \tag{16}$$

where P (Pa) is the pressure, μ_B (Pa.s) is the gas viscosity, ρ_B (kg.m^{-3}) is the fluid density, z (m) is the bed length coordinate, and u (m.s^{-1}) is the superficial gas flow velocity, which depends on the pressure and the velocity of the feed, as described by:

$$u = \left(\rho_B u_{\text{feed}}\right) / \rho = u_{\text{feed}} P_{\text{feed}} / P \tag{17}$$

The validity of this relationship is based on several assumptions: a constant flow rate throughout the column, an isothermal system, and the behavior of the fluid as an ideal gas. It is important to note that the initial and boundary conditions mentioned refer specifically to the adsorption stage of the pressure swing adsorption (PSA) process. Other conditions are required for other operating steps such as pressurization, blowdown, and purging. Depending on the operating step, the steep front of the breakthrough curve can propagate either from z=0 to L or in the opposite direction. Because of the reversible nature of the process, we can treat the desorption breakthrough curve like an adsorption breakthrough curve. The only differences are in the initial and boundary conditions. Therefore, we can use the same model as described above with the initial and boundary conditions modified as [24]:

$$* t = 0 \qquad c = c_0,\ c_{pe} = c_{pe|_{r_p = r_{pe}}},\ \bar{q} = q_e, \quad \forall z \text{ and } r_p \tag{18}$$

$$* z = 0 \qquad \frac{\partial c}{\partial z} = 0,\ \forall t \text{ and } r_p \tag{19}$$

Table *4* summarizes the correlations employed to estimate the parameters of the Fickian multiscale model.

Table 4: Correlations for estimating parameter model

Molecular diffusion, D_{AB}, (m^2.s^{-1}) [25,26]	$D_{AB} = 2.6628\times10^{-22}\dfrac{\sqrt{T^3\dfrac{M_A+M_B}{2\times10^3 M_A M_B}}}{p_t \sigma_A \sigma_B \Omega_D}$ with: $\Omega_D = b_1\left(\dfrac{T}{\varepsilon_k}\right)^{b_2} + b_3\exp^{\left(-b_4\frac{T}{\varepsilon_k}\right)} + b_5\exp^{\left(-b_6\frac{T}{\varepsilon_k}\right)} + b_7\exp^{\left(-b_8\frac{T}{\varepsilon_k}\right)}$ where: $b_1 = 1.060;\ b_2 = 0.156;\ b_3 = 0.193;\ b_4 = 0.476;$ $b_5 = 1.036;\ b_6 = 1.529;\ b_7 = 1.765;\ b_8 = 3.894;\ \varepsilon_k = \sqrt{\varepsilon_A \varepsilon_B / k_b{}^2};$ $\varepsilon_A / k_b = 809.1;\ \varepsilon_B / k_b = 97;\ \sigma_A = 2.641\times10^{-10};\ \sigma_B = 3.617\times10^{-10}$

Dynamic viscosity, μ_B (Pa.s) [26]	$\mu_B = 2.669\times10^{-6}\frac{\sqrt{T(M_B)10^3}}{{\sigma_B}^2\Omega_D}$ with: $\Omega_D = b_1\left(\frac{T}{\varepsilon_B/k_b}\right)^{b_2} + b_3\exp^{\left(-b_4\frac{T}{\varepsilon_B/k_b}\right)} + b_5\exp^{\left(-b_6\frac{T}{\varepsilon_B/k_b}\right)} + b_7\exp^{\left(-b_8\frac{T}{\varepsilon_B/k_b}\right)}$
Knudsen diffusion, D_K (m².s-1) [26]	$D_K = \frac{4}{3}r_{mp}\sqrt{\frac{2R_gT}{\pi M_A}}$
Effective diffusion, D_e (m².s-1)	$D_e = \varepsilon_{pe}\frac{D_M}{\tau_{pe}}$ with: $D_M = \left(\frac{1}{D_{AB}} + \frac{1}{D_K}\right)^{-1}$ where: $\tau_{pe} = \varepsilon_{pe}^{-1/3}$
External film mass transfer coefficient, k_f (m.s-1), [27]	$k_f = \frac{D_{AB}Sh}{d_{pe}}$ with: $Sh = c_{m_1} + c_{m_2}\,\mathrm{Re}^{0.6}\,Sc^{1/3}; 3 < \mathrm{Re} < 10^4$ $Sc = \frac{\mu_B}{\rho_B D_{AB}}; Re_p = \frac{\rho_B d_{pe} u}{\mu_B}$ where: $c_{m_1} = 2$ and $c_{m_2} = 1.1$
Axial dispersion coefficient, D_{ax} (m².s-1) [28]	$D_{ax} = \frac{vd_{pe}}{Pe'}$ with: $\frac{1}{Pe'} = \frac{0.7D_{AB}}{d_{pe}v} + \frac{\varepsilon_b}{c_{m_3} + c_{m_4}(Re_p)^{0.59}}$ where: $c_{m_3} = 0.18$ and $c_{m_4} = 0.008$
Gaz density, ρ_B (kg.m-3)	$\rho_B = \frac{PM_B}{R_gT}$
Local slope, k_{pe} (see section 2 of SI)	$k_{pe} = \frac{\partial q_e^*}{\partial c} = \rho_s q_m b\left[1+(bc)^{t_o}\right]^{-\frac{1+t_o}{t_o}} = 1.2\times10^5$

The resulting model (equations 6 through 19) is analyzed, identified, and validated using experimental measurements. The initial values used to fit the model were estimated from the literature and are listed in Table *4*. Fitting with these initial values did not give good agreement with the experimental measurements, indicating that the parameters should be estimated. Even if some parameters can be estimated theoretically, there may be experimental uncertainties that can affect their accuracy. Therefore, fitting the experimental measurements to the predictions can help determine the actual values of these parameters, which cannot be easily measured or estimated. In addition, simulation can provide insight into the behavior of the system under different conditions, which can be useful for optimizing the process. Overall, the combination of experimental and simulation-based approaches is often necessary to obtain a complete understanding of the system behavior and to optimize the process. Since the coefficient of external mass transfer and axial dispersion increase with gas flow rate, the parameters c_{m2}, c_{m3}, and c_{m4} (see Table *4*) included in the correlation of Wakao and Funazkri and Rastegar and Gu

[27,28] are estimated to maintain the same trend. The model includes several unknown parameters that must be estimated from the measurements, including k_1, c_{m2}, c_{m3}, c_{m4}, and D_M. To determine the optimal values (p^*) of these estimable parameters (p^{est}), a constrained optimization problem is solved as follows:

$$p^* := \arg\min_{P^{est}} \sum_{j=1}^{k} \sum_{i=1}^{n_m} \left(c_i \Big|_j - \hat{c}_i \Big|_j \right)^2 \tag{20}$$

subjected to:

$$p_{\min}^{est} \le p^{est} \le p_{\max}^{est} \tag{21}$$

where c_i and $\hat{c}_i$ are the measured and predicted concentration values, k represents the number of operating conditions (flow rates and initial concentrations), and n_m is the number of measurements. The optimization algorithm employed in this study utilizes the moving asymptote (MMA) method, which is available within the COMSOL Multiphysics® software. The identified parameters' accuracy is assessed through the use of confidence intervals (*CI*), as follows [26]:

$$p^*_{1-\alpha_t} = p^* \pm t_{s\left(n_m - n_p, \alpha_t/2\right)} \sqrt{diag(COV(p^*))} \tag{22}$$

with:

$$COV(p^*) \approx \frac{J^{mse}}{n_m - n_p} \left(J(p^*)^T J(p^*) \right)^{-1} \tag{23}$$

The confidence intervals (*CI*) for the estimated parameters are determined using the covariance matrix (*COV*), which takes into account the Student t-distribution ($t_{s\left(n_s - n_p, \alpha_t/2\right)}$) corresponding to the significance level $\alpha_t / 2$ and (n_m-n_p) degrees of freedom. Here, n_p represents the number of parameters, and J denotes the Jacobian matrix of the residual vector (r_v), which quantifies the difference between the model predictions and the measured values. Mathematically, it can be expressed as:

$$J = \begin{bmatrix} \frac{\partial r_{v_1}}{\partial p_1} & \cdots & \frac{\partial r_{v_1}}{\partial p_{n_p}} \\ \vdots & \ddots & \vdots \\ \frac{\partial r_{v_{n_s}}}{\partial p_1} & \cdots & \frac{\partial r_{v_{n_s}}}{\partial p_{n_p}} \end{bmatrix} \tag{24}$$

The performance of the model predictions is assessed using two key indices: the root means square error (*RMSE*) and the Pearson correlation coefficient. The RMSE quantifies the average difference between the model predictions and the experimental measurements. It is calculated as follows:

$$RMSE = \sqrt{\frac{1}{n_m k}\sum_{j=1}^{k}\sum_{i=1}^{n_m}\left(c_i\big|_j - \hat{c}_i\big|_j\right)^2} \tag{25}$$

The Pearson correlation coefficient measures the strength and direction of the linear relationship between the model predictions and the experimental measurements. It is expressed as [29]:

$$r = \frac{\sum_{j=1}^{k}\sum_{i=1}^{n_m}\left(c_i\big|_j - \overline{c}_i\big|_j\right)\left(\hat{c}_i\big|_j - \overline{\hat{c}}_i\big|_j\right)}{\sqrt{\left(\sum_{j=1}^{k}\sum_{i=1}^{n_m}\left(c_i\big|_j - \overline{c}_i\big|_j\right)^2\right)\left(\sum_{j=1}^{k}\sum_{i=1}^{n_m}\left(\hat{c}_i\big|_j - \overline{\hat{c}}_i\big|_j\right)^2\right)}} \tag{26}$$

where $\overline{c}$ and $\overline{\hat{c}}$ are the mean values of the measured and predicted, respectively.

4. Results and discussion

The experimental data used consist of breakthrough curve measurements carried out at a room temperature of 20 °C, five different relative humidities of 15, 30, 45, 60, and 70% *RH* or water vapor concentrations of 0.14, 0.29, 0.44, 0.58, and 0.72 mol.m^{-3}, and three gas flow rates of 170, 135, and 100 mL.min^{-1}, i.e., fifteen adsorption and desorption experimental measurements to identified parameters. The relative humidity remained below 80% during the experiments, which ensured that the system did not enter the condensation zone. It is important to note that the model and subsequent results presented in this study are applicable and valid within this range of relative humidity. Above the condensation zone, the behavior of water vapor in the confined spaces of adsorbent pores may be significantly different due to the potential for condensation. The assumption of ideal gas behavior and the applicability of the adsorption and desorption equations may no longer be valid under these conditions. Therefore, the validity and predictions of the model are limited to the studied range of relative humidity below the condensation zone. With the available experimental measurements, the parameters D_M, c_{m2}, k_1, c_{m3} and c_{m4} were estimated. However, the desorption breakthrough curve was treated in the same way as that of adsorption, i.e., (c_0-c) was used to obtain a classical *S*-type adsorption breakthrough curve. This method is possible if the adsorption and desorption processes are reversible, which is justified by

the observation of the isotherm of water vapor on alumina [5,18,30,31], where capillary condensation is not achieved, confirming that the desorption branch follows the adsorption branch. The assumption that k_1 for adsorption and desorption should be equal is a common assumption in adsorption and desorption models. However, further examination and comparison of experimental breakthrough curves with our model predictions revealed that this assumption was not entirely accurate in this study. Moreover, in the capillary condensation region, the adsorption and desorption breakthrough behaviors differ from each other [32–34]. This is due to the fact that in this region, the pores of the adsorbent fill with water molecules, which leads to a decrease in the available adsorption sites. As a result, the adsorption capacity of the adsorbent decreases while the desorption capacity increases. As the water vapor concentration increases beyond the inflection point of the isotherm, the adsorption capacity of the adsorbent becomes increasingly limited and desorption becomes more critical. Therefore, the optimal parameters identified and estimated during adsorption are used in the desorption simulation, except for the parameter k_1, which is estimated simultaneously from available desorption experimental measurements. Figures *2* and *3* compare the experimental measurements to the model predictions obtained using the optimized parameters in the adsorption and desorption process. The water vapor/alumina isotherm model used is the Toth-Aranovich-Donohue.

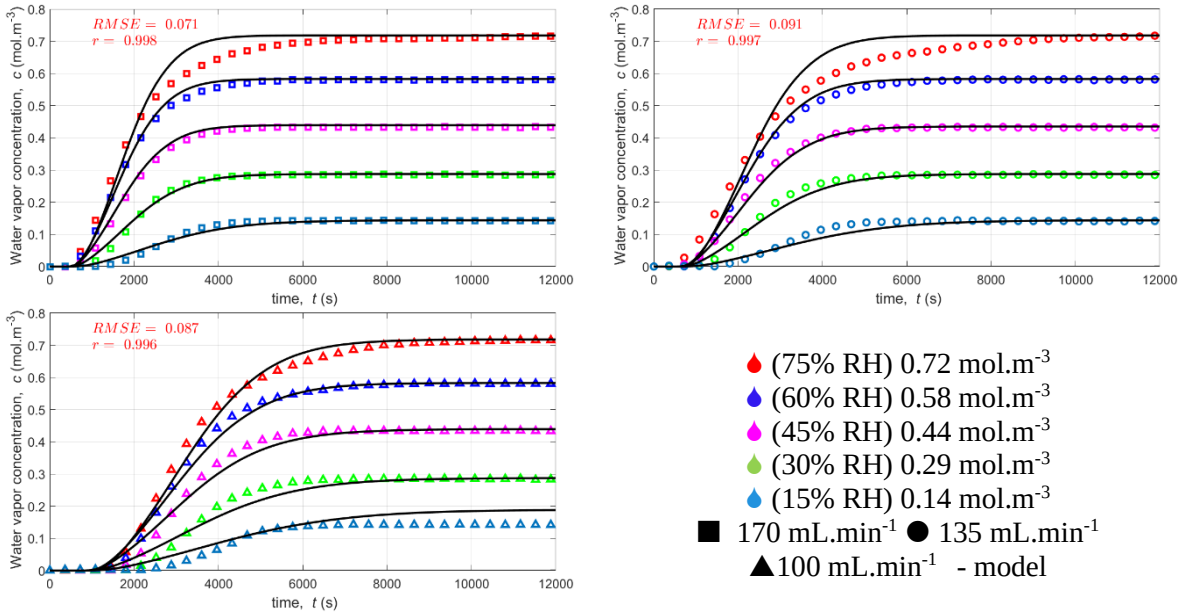

Figure 2: Comparison of water vapor adsorption breakthrough curves on alumina predicted with the experimental measurements using the multiscale model.

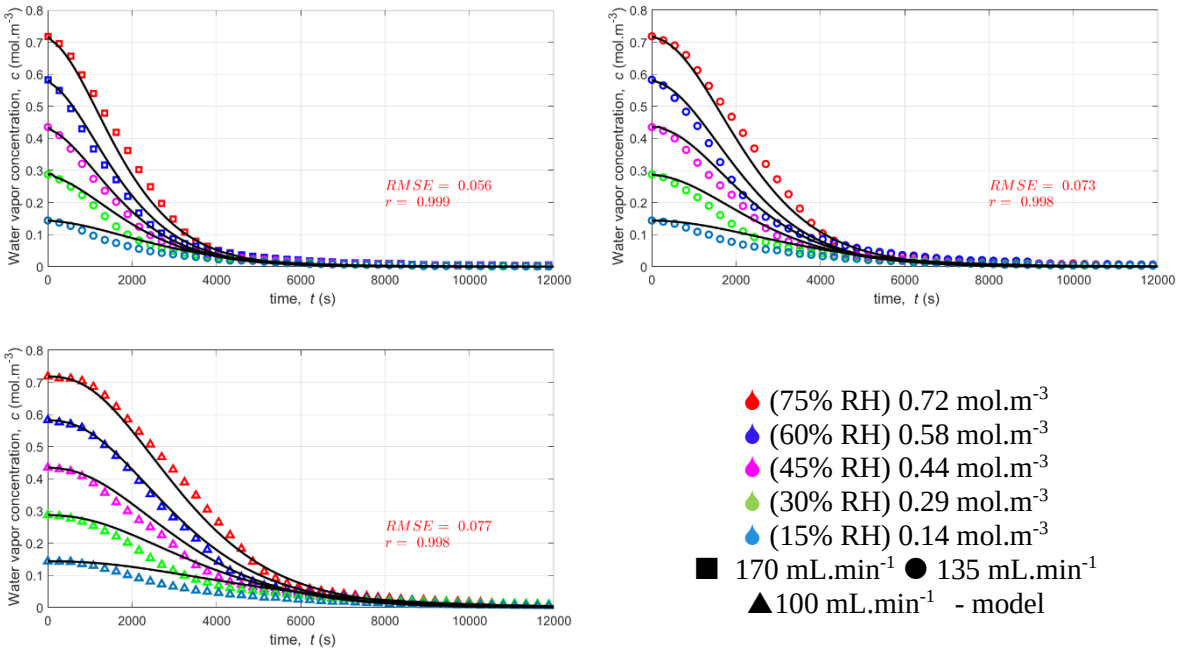

Figure 3: Comparison of desorption breakthrough curves predicted with the experimental measurements using the multiscale model.

The optimized parameter values as well as their 95% confidence intervals (*CI*), and the dimensionless material Biot number (B_i) of is reported in the Table *5*.

Table 5: Optimized parameter values for water vapor adsorption on alumina

B_i=4.63					*Adsorption*	*Desorption*
Parameters	c_{m2}	c_{m3}	c_{m4}	D_M, ($m^2.s^{-1}$)	$k_{1,ads}$ (s^{-1})	$k_{1,des}$ (s^{-1})
Value	5.93	0.005	1.01×10^{-5}	4.3×10^{-5}	0.065	0.0018
CI (95%)	±1.26	±0.002	$\pm 0.9 \times 10^{-6}$	$\pm 8.5 \times 10^{-6}$	±0.005	±0.0006

Figures *2* and *3* demonstrate the strong agreement between the predictions of the multiscale model and the experimental measurements, as evidenced by the high Pearson correlation coefficient (r=0.99) and the small root mean square error ($RMSE$<0.09). The fast saturation of the adsorbent bed at higher flow rates can be attributed to the reduction in film thickness surrounding the particles. As the flow rate increases, the thinner film enhances mass transfer by reducing its resistance value. The value of the material Biot number (see Table *5*) is greater than 3. Therefore, the adsorption mechanism is controlled by internal pore diffusion. Moreover, the breakthrough time, defined as the time required to reach 10% of the water vapor concentration in the bed column, decreases with increasing water vapor concentration at the inlet. It can also be observed that an increase in water vapor concentration at the inlet results in bed saturation being reached earlier due to relatively faster transport. Since the confidence interval

values are lower than the parameter values reported in Table *5*, the parameter identification can be considered accurate given the excellent fit indices. The coefficients for external film mass transfer and axial dispersion could be estimated with a different correlation than the one used, for example, by Athalye et al [35], Delgado[36] and Valdés-Solís et al [37] to improve the agreement between measurements and predictions. Despite this discrepancy, the estimated coefficients reported in Table *6* for different gas flow rates are in line with the magnitudes commonly reported in the literature [38,39]. Water vapor molecules are adsorbed in the pores (meso and macro) by forming hydrogen bonds between the adsorbed molecules and the adsorbent surface. The isosteric heat generated is 46 kJ/mol [18], indicating a strong interaction between the water vapor molecule and the alumina surface. As a result, the desorption process is endothermic and requires additional heat or pressure to release the molecules. In this study, desorption is performed under the same conditions as adsorption without external (energy) input, suggesting that it is easier to release the adsorbed molecules in macropores than in mesopores. This difference is reflected in the observed internal mass transfer coefficients, which differ by a factor of 36 for adsorption and desorption in mesopores. It should be noted the variation in velocity and pressure drop were found to be negligible and equation 17 was found to be unnecessary. However, it is included in analysis as a precautionary measure for the consideration of high-pressure industrial columns that may experience significant pressure drops. According to reference book Pressure Swing Adsorption by of D.M. Ruthven et al. [40] adsorption of water can lead to changes in the velocity of the adsorbent which can impact the performance of the process. Therefore, it is essential to consider the effects of water adsorption on velocity in any analysis of adsorption processes. The adsorption and desorption kinetics within an adsorbent particle can be influenced by various transfer mechanisms, including external mass transfer, porous diffusion, and internal diffusion. The relative significance of these mechanisms depends on the specific adsorption system. To assess the importance of each transfer mechanism, the concept of characteristic time [41] is commonly employed. These characteristic times are estimated by calculating the dynamic response times of the adsorption and desorption processes. Table *6* provides the characteristic times associated with mass transfer resistances for reference.

Table 6: Axial dispersion and external film mass transfer coefficients values and characteristic times of different mass transfer resistances at different gas flow rates

Q_v mL.min^{-1}	D_{ax} m^2.s^{-1}	k_f m.s^{-1}	t_{kf} $\times 10^{-4}$ s	t_{macro} $\times 10^{-3}$ s	$t_{meso,ads}$ $\times 10^{-4}$ s	$t_{meso,des}$ $\times 10^{-3}$ s
170	0.05	0.56	7.6	7.1	1.5	5.4
			5.7%	52.9%	1.3%	40.1
135	0.04	0.49	8.7	7.1	1.5	5.4
			6.4%	52.5%	1.1%	39.9%
100	0.03	0.41	10.1	7.1	1.5	5.4
			7.6%	52.0%	1.1%	39.6%

$$t_{k_f} = \frac{r_{pe}^{\ 2}}{3k_f}; t_{macro} = \frac{r_{pe}^{\ 2}}{15D_e}; t_{meso,ads} = \frac{r_{mp}^{\ 2}}{15k_{pe}D_{meso,ads}}; t_{meso,des} = \frac{r_{mp}^{\ 2}}{15k_{pe}D_{meso,des}}$$

The characteristic times for the different transfer mechanisms in the adsorption and desorption processes are defined as follows: $t_{meso,ads}$ (s) represents the characteristic time for mesopore diffusion during adsorption, $t_{meso,des}$ (s) represents the characteristic time for mesopore diffusion during desorption, t_{kf} (s) represents the characteristic time for external film mass transfer, and t_{macro}(s) represents the characteristic time for macropore diffusion. As shown in Table *6*, the overall resistance of adsorption and desorption mass transfer is controlled 50% by macropore diffusion transport and 40% by mesopore diffusion in the desorption process. In other words, the adsorption process is controlled by the diffusion of water vapor into the macropores, while the desorption process is controlled by the diffusion of water vapor into the macropores and mesopores. This analysis of the resistances justifies the fact that during an adsorption and desorption cycle, the desorption process takes more time than the sorption process. The external transfer resistance controls the remaining 10% in the adsorption and desorption process. The total relative mass transport contributions for adsorption and desorption using HTEP method are used (See section *4* of the supplementary information for details), were found to be 2.818 and 2.858 respectively. As seen in the calculation of the time transport resistances in Table 6, the adsorption process shows a significant contribution from relative mass transport resistances (without considering axial dispersion contribution) in macropores (76%), while the desorption process exhibits a noteworthy contribution from transport in both mesopores (68%) and macropores (26%). The equilibrium dynamic adsorption capacity of the bed, as a function of the inlet concentration, is determined from the

breakthrough curves shown in Figures *2* and *3*. This is achieved through a mass balance calculation, is determined using the following equation [42]:

$$q_{ad} = \frac{Q_v c_0}{m_{AD}} t_{st} \text{ with: } t_{st} = \int_{t_0}^{t_f} \left[1 - \frac{c_{(t)}}{c_0} \right] dt \quad (27)$$

In this equation, q_{ad} (mol.kg^{-1}) represents the water vapor adsorbed in the bed, m_{AD} (kg) is the mass of adsorbent charged into the column, t_{st} (s) is the time equivalent to the total or stoichiometric capacity of the bed, Q_v (m^3.s^{-1}) is the gas flow rate, c_0 (mol. m^{-3}) is the inlet water vapor concentration, t_0 and t_f (s) are the initial and final times of the dynamic adsorption measurements, and $c_{(t)}$ (mol.m^{-3}) represents the water vapor concentration at time *t*. The estimated values of the amount of water vapor dynamically adsorbed as a function of water vapor concentration for each gas flow rate for adsorption and desorption were compared with the predictions of the isotherm model for alumina in Figure *4*.

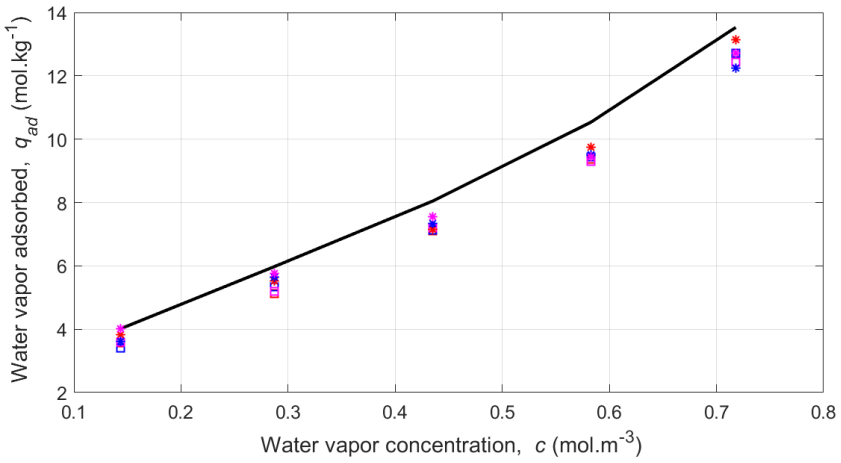

170 mL.min^{-1}, 135 mL.min^{-1}, 100 mL.min^{-1}

* Adsorption □Desorption – Toth Aranovich Donohue isotherm model

Figure 4: Comparison of the water vapor amount adsorbed from the adsorption and desorption experimental breakthrough curves on alumina for each flow rate to the isotherm model predictions

Figure *4* shows that the values of adsorbed water vapor quantity estimated from the experimental breakthrough curves are close to those obtained from the isotherm model predictions, with a deviation of less than 10%, which corresponds to the measurement errors of the devices. These results indicate that the isothermal measurements of water vapor adsorption were made accurately and that the predictions of the isothermal model are correct. Since the values obtained for the amount of water vapor

adsorbed during adsorption and desorption are close, it can be confirmed that the process is reversible, i.e., that the water vapor is physically adsorbed onto alumina.

5. Model Validation

For a model to be fully validated, it shall have good performance indices and satisfy a statistical test such as the nonparametric Kolmogorov-Smirnov test [43]. The fit between the predicted and measured breakthrough curves is assessed using three performance indices: the agreement index (*IA*), the modified agreement index (*IAM*), and the chi-squared error. The agreement index (*IA*), represented by Equation (28), measures the mean square error and potential error. It has a range of 0 to 1, with higher values indicating a stronger correlation between the measured and predicted values [44].

$$IA = 1 - \frac{\sum_{i=1}^{n_m} \left(c_i - \hat{c}_i\right)^2}{\sum_{i=1}^{n_m} \left(\left|c_i - \bar{c}_i\right| + \left|\hat{c}_i - \bar{\hat{c}}\right|\right)^2} \tag{28}$$

To mitigate the impact of quadratic terms, the modified agreement index (*IAM*) is proposed by Willmott et al, defined as:

$$IAM = 1 - \frac{\sum_{i=1}^{n_m} \left|c_i - \hat{c}_i\right|}{\sum_{i=1}^{n_m} \left|c_i - \bar{c}_i\right| + \left|\hat{c}_i - \bar{\hat{c}}_i\right|} \tag{29}$$

Furthermore, the chi-squared error [45], calculated according to Equation (30), compares the distributions between the measurements and the model predictions, providing a non-linear assessment.

$$\chi^2 = \sum_{i=1}^{n_m} \frac{\left(c_i - \hat{c}_i\right)^2}{c_i} \tag{30}$$

For validation, the identified model is tested using additional measurements of water vapor adsorption and desorption breakthrough curves on hopcalite. These measurements are conducted at gas flow rates of 90, 120, and 150 mL.min^{-1} with a water vapor concentration of 0.67 mol.m^{-3} (or a relative humidity of 70%), as well as at a gas flow rate of 135 mL.min^{-1} with three water vapor concentrations of 0.38, 0.48, and 0.77 mol.m^{-3} (or relative humidities of 40, 50, and 80%). These conditions differ from those used for parameter identification. The optimized parameter values listed in in Table *5* are employed to

simulate these curves. Figure 5 illustrates the comparison between the predicted and measured curves, considering a room temperature of 20 °C, different gas flow rates, and various water vapor concentrations. The water vapor/hopcalite isotherm model used is the Toth-Aranovich-Donohue.

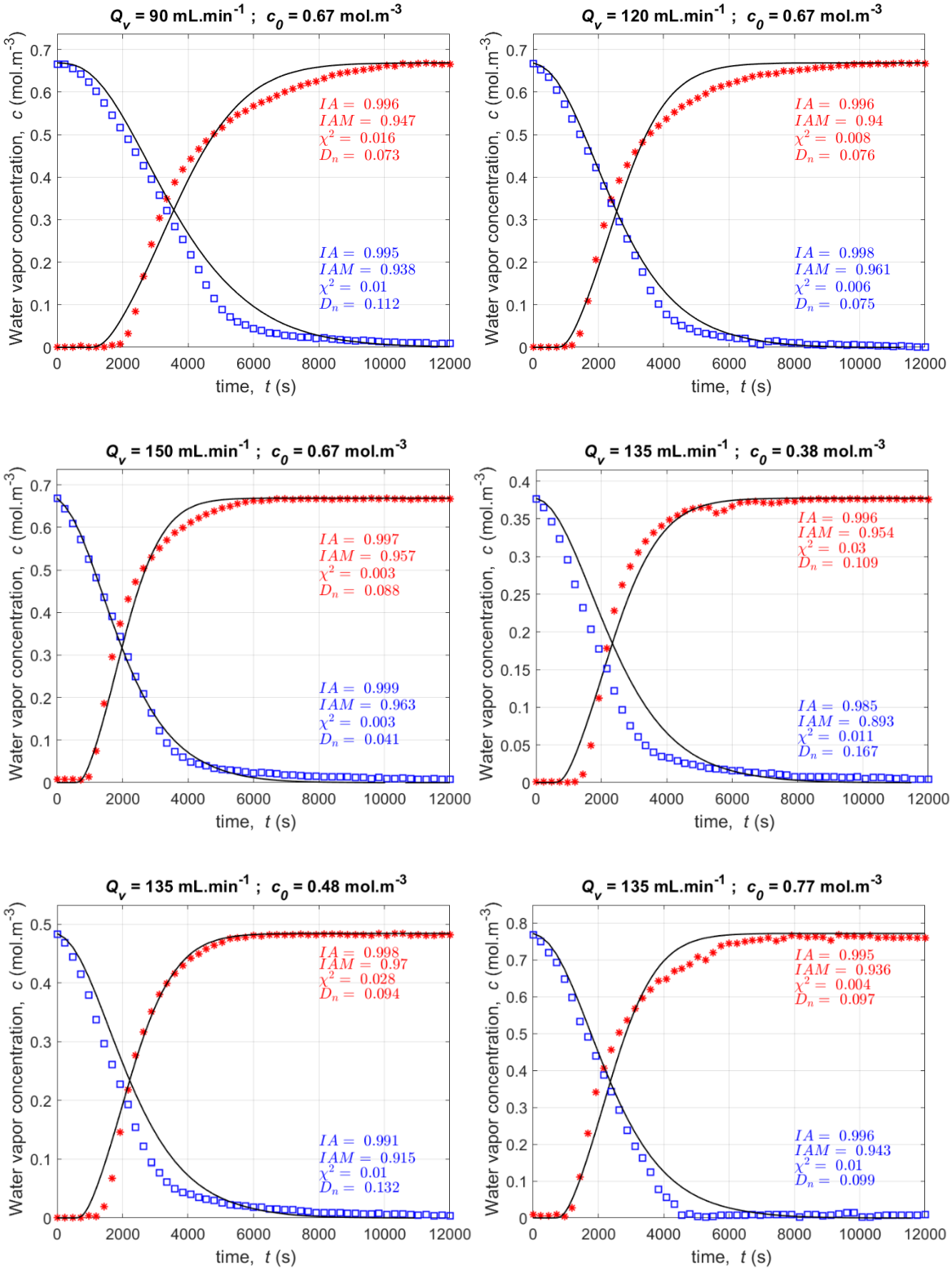

Figure 5: Comparison between predicted and measured breakthrough curves on hopcalite at three gas flow rates 90, 120 and 150 mL.min^{-1} with a water vapor concentration of 0.67 mol.m^{-3}; and at a gas flow rate of 135 mL.min^{-1} with three water vapor concentrations of 0.38, 0.48, and 0.77 mol.m^{-3}.

Based on the results presented in Figure 5, the performance indices *IA* and *IAM* have values close to unity. Moreover, the low chi-squared error value confirms the exceptional agreement between the model predictions and the measured for the water vapor adsorption and desorption breakthrough curves on hopcalite. To obtain a comprehensive evaluation of the agreement between the model predictions and the measurements, the Kolmogorov-Smirnov statistical test is applied. This statistical test consists in estimating the divergence (D_n) between two distributions, namely the ($\hat{c}_{(t)}$) and measured ($c_{(t)}$) values of water vapor concentration at each time *t*, defined as follows [43]:

$$D_n = \max_t \left| c_{(t)} - \hat{c}_{(t)} \right| \tag{31}$$

The estimated divergence values, which are below the critical value, allow the acceptance of the null hypothesis (H0), i.e., with a confidence level of 95%, it can be stated that the predicted and the measured breakthrough curves have the same distribution. Based on the results shown in Figure 5, the predictions of the water vapor adsorption model consistently confirm this null hypothesis, so we can confidently confirm the ability of the multiscale model to accurately predict water vapor adsorption on alumina and hopcalite. On the other hand, the predictions of the water vapor desorption model are guaranteed at high gas flow rates and concentrations. This fact is justified because the water vapor adsorption isotherms on alumina and hopcalite are similar at high concentrations but not at low concentrations. In addition, the measurement errors of the instruments increase at low concentrations, which means that the prediction of the model is not as good at low concentrations. These errors can be caused by factors such as instrument sensitivity, calibration, and measurement noise. As the adsorbate concentration decreases, the measurement errors of the instruments may become more pronounced, leading to a decrease in the accuracy of the model predictions. This could be related to the techniques used for concentration measurement, which are not sensitive enough or not able to detect low concentrations, leading to error. In addition, the model may not be able to accurately capture the effects of adsorbate-adsorbent interactions at low concentrations. It is important to test the model under various conditions to validate its accuracy and understand the limitations of the model under certain conditions.

6. Implementation of model validation

The aim of this study is to develop a predictive model for adsorption and desorption breakthrough curves considering factors such as concentration, flow rate, and temperature. To achieve this, the validated model was used to predict the adsorption and desorption breakthrough curves on alumina while maintaining a constant water vapor pressure of 1.18 kPa. The predictions were made at different temperatures, namely 50, 40, 30, and 20 °C, corresponding to water vapor concentrations of 0.44, 0.45, 0.47, and 0.48 mol.m^{-3}, respectively. The gas flow rate used for these predictions was set at 200 mL.min^{-1}. The results are shown in Figure *6*. It should be noted that these operating conditions (concentration, gas flow rate, and temperature) are different from those used for parameter identification and model validation.

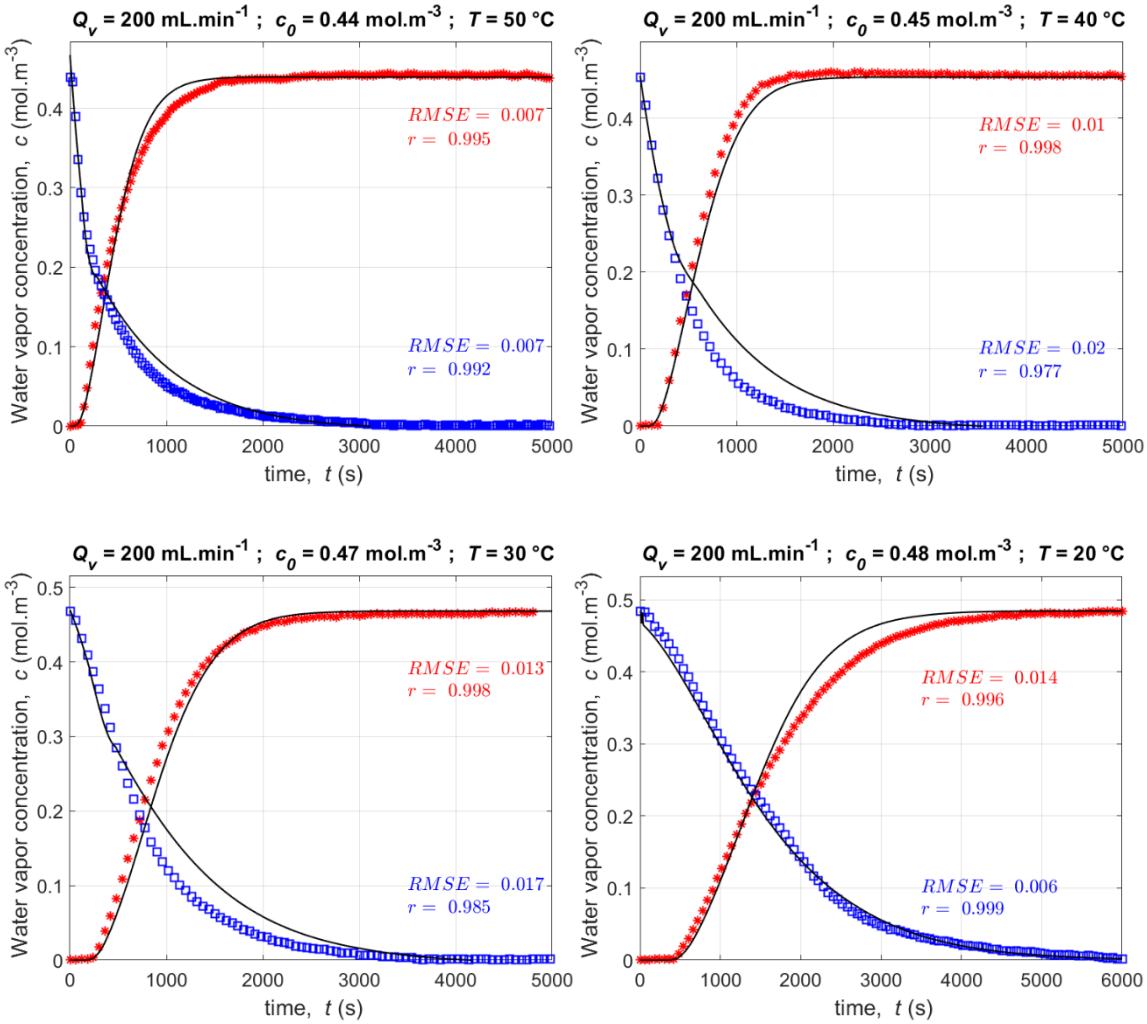

Figure 6: Comparison between predicted and measured breakthrough curves on alumina at four temperatures of 50, 40, 30, and 20 °C corresponding to water vapor concentrations of 0.44, 0.45, 0.47, 0.48, mol.m^{-3} and a gas flow rate of 200 mL.min^{-1}.

Figure *6* shows that the adsorption breakthrough time, typically defined as the time required to reach 10% of the initial concentration, decreases from 800 to 200 s as the temperature increases from 20 to 50 °C. This discrepancy occurs when the concentration gradient between the film and the particle approaches equilibrium and the particle is near equilibrium, or when the water vapor concentration in the material pores is lower. The reason for this discrepancy is the use of the LDF equation with linear driving force for the mass balance in the micropores of the particles, which could be improved by a Fickian diffusion-transport equation [46]. However, the nearly uniform value of the Pearson correlation coefficient and a low *RMSE* confirm the excellent agreement between model predictions and measurements, which is due to the fact that a temperature-dependent isotherm model such as the Toth-Aranovich-Donohue model was used in the implementation of the validated model. The identified, validated, and implemented multiscale model can serve as a valuable tool for studying the effects of different operating conditions and predicting the breakthrough time of water vapor in a bed column filled with alumina and/or hopcalite.

7. Conclusions

The accuracy of the one-dimensional adsorption and desorption model using the temperature-dependent Toth-Aranovich-Donohue equation developed, identified, validated, and implemented for the simulation of a packed bed column in which water vapor is physically adsorbed on alumina and hopcalite was demonstrated. The fickian multiscale model allowed the finding that the adsorption process is controlled by the diffusion of water vapor in the macropores. In contrast, the desorption process is controlled by water vapor diffusion in the macropores and mesopores. This statement is based on the study of a specific adsorbent (alumina/hopcalite) and adsorbate (water vapor). A sufficient number of breakthrough curve measurements were used simulatively to estimate mass transport coefficients to determine the relative contributions of the HTEP method and characteristic times to reach a valid conclusion. Furthermore, the analysis of the pore size distribution and the experimental isotherm of the II types confirm the statement reached. This fact was also confirmed by a value of the material Biot

number higher than 3, which means that the process is controlled by the internal pore diffusion transport. The advantage of our multiscale model over the classical LDF model is the quantitative estimation of the resistances of the adsorption and desorption processes. The LDF model does not allow us to distinguish the coefficients for external film mass transport, pore diffusion, and internal mass transport because all resistances are lumped in one global coefficient. The statistical validation and the performance of the model indices ensure the quality of the model predictions, which is not always the case in modeling studies. This model coupled with an energy balance to improve the design and optimization of commercial adsorption columns with multilayer beds. The one-dimensional model is a common and widely accepted simplification often used in adsorption studies. The rationale for this assumption is that the column is sufficiently long and narrow so that the flow is in only one direction and lateral dispersion can be neglected. This allows for a simpler mathematical treatment of the transport phenomena and facilitates the identification and estimation of the model parameters. However, it is also important to note that the validity of the one-dimensional model should be assessed on a case-by-case basis, depending on the specific system under study. In our study, we considered a long, narrow column with a relatively simple geometry and carefully controlled the flow conditions to minimize lateral dispersion. We also compared and validated our simulation results with experimental measurements and found good agreement, suggesting that the one-dimensional model is a reasonable simplification for our system. Nevertheless, we acknowledge that the one-dimensional model is a simplification of the real system and may not fully capture all hydrodynamic effects. In future studies, we plan to investigate the effects of boundary effects and preferred pathways on the system and refine our model accordingly.

Nomenclature

b_0, b_{20} Equilibrium constants at low and high concentrations at T_0 (mol.m^{-3})

B_i Material Biot number

$c_i, \hat{c}_i$ Measured and predicted water vapor concentration (mol.m^{-3})

c_{m1}, c_{m2} Constants to estimate the external film mass transfer coefficient

c_{m3}, c_{m4} Constants to estimate the axial dispersion coefficient

c_0 Initial water vapor concentration (mol.m^{-3})

c_{pe} Water vapor concentration in the particle (mol.m^{-3})

$c_{pe|r_p=r_{pe}}$ Water vapor concentration at the particle surface (mol.m^{-3})

D_{meso} Mesopore diffusion coefficient (m².s^{-1})

D_{n*} Critical divergence value

D_{ax} Axial dispersion coefficient (m².s^{-1})

D_e Effective diffusion coefficient (m².s^{-1})

D_M Mixture diffusion coefficient (m².s^{-1})

IA(M) Index of agreement (modified)

k_1 Internal mass transfer coefficient (s^{-1})

k_b The Boltzmann constant (J.K^{-1})

k_{pe} Local slope

M_A Molecular weight of water vapor (kg.mol^{-1})

M_B Molecular weight of air (kg.mol^{-1})

Pe' Péclet number

n_2 Constant parameter in the Toth-Aranovich–Donohue equation

P Pressure (Pa)

$\boldsymbol{p}$ Vector of parameters

q_e Water vapor amount adsorbed (mol.kg^{-1})

q_{m0} Maximum amount adsorbed at T_0 (mol.kg^{-1})

Q Heat of adsorption at the monolayer (J.mol^{-1})

Q_2 Heat of adsorption at the multilayer (J.mol^{-1})

Q_v Gaz flow rate (L.min^{-1})

r Pearson correlation coefficient

R_{ep} Particle Reynolds number

R_g Ideal gas constant (J.mol^{-1}.K^{-1})

$RMSE$ Root mean square error

t_{o0} Heterogeneity factor the Toth-Aranovich–Donohue equation at T_0

T Temperature (K)

T_0 Reference temperature (K)

u Superficial gas flow velocity (m.s^{-1})

v Interstitial gas flow velocity (m.s^{-1})

Greek letters

α Constant parameter the Toth-Aranovich–Donohue equation

α_t Level of significance

ΔH Isosteric heat of adsorption (J.mol^{-1})

ε_b Bed porosity

ε_{pe} Particle porosity

μ_B Air dynamic viscosity (Pa.s)

ρ_s Solid density (kg.m^{-3})

σ_A, σ_B Characteristic length of the Lennard-Jones potential (m)

τ_{pe} Tortuosity in the particle

χ^2 Chi-square error

Associated Content

Supporting information: Reduced column, Local slope, Pore size distribution, Water vapor adsorption isotherms, Relative mass transport resistances contributions.

Author Information

Corresponding author

Cristian Cardenas, Université Claude Bernard Lyon 1, CNRS-IRCELYON, 69626 Villeurbanne, France, https://orcid.org/0000-0002-4135-7415, Phone: +33472445365, Email: cristian.cardenas@ircelyon.univ-lyon1.fr

Authors

David Farrusseng, Université Claude Bernard Lyon 1, CNRS-IRCELYON, 69626 Villeurbanne, France, https://orcid.org/0000-0002-9093-4143, Email: david.farrusseng@ircelyon.univ-lyon1.fr

Cécile Daniel, Université Claude Bernard Lyon 1, CNRS-IRCELYON, 69626 Villeurbanne, France, https://orcid.org/0000-0003-4560-9242, Email: cecile.daniel@ircelyon.univ-lyon1.fr

Competing interests

The authors have no relevant financial or non-financial interests to disclose.

Funding

No funding was received to assist with the preparation of this manuscript.

Availability of data and materials

Data will be made available on request.

Acknowledgments

The authors acknowledge financial support from the National Research Agency (ANR) as part of the France Relance plan.

8. References

(1) Ackley, M. W. Medical Oxygen Concentrators: A Review of Progress in Air Separation Technology. *Adsorption*. Springer New York LLC November 1, 2019, pp 1437–1474. https://doi.org/10.1007/s10450-019-00155-w.

(2) Normes internationales ISO. ISO 7396-1:2016 Medical Gas Pipeline Systems - Part 1 : Pipeline Systems for Compressed Medical Gases and Vacuum. 2-01/03/2020, 2016.

(3) Murali, R. S.; Sankarshana, T.; Sridhar, S. Air Separation by Polymer-Based Membrane Technology. *Sep. Purif. Rev.* **2013**, *42* (2), 130–186. https://doi.org/10.1080/15422119.2012.686000.

(4) Carter, J. W.; Wyszynski, M. L. The Pressure Swing Adsorption Drying of Compressed Air. *Chem. Eng. Sci.* **1983**, *38* (7), 1093–1099. https://doi.org/10.1016/0009-2509(83)80030-X.

(5) Serbezov, A. Adsorption Equilibrium of Water Vapor on F-200 Activated Alumina. *J. Chem. Eng. Data* **2003**, *48* (2), 421–425. https://doi.org/10.1021/je025616d.

(6) Pui, W. K.; Yusoff, R.; Aroua, M. K. A Review on Activated Carbon Adsorption for Volatile Organic Compounds (VOCs). *Reviews in Chemical Engineering*. De Gruyter July 1, 2019, pp 649–668. https://doi.org/10.1515/revce-2017-0057.

(7) Brittan, M. I.; Bliss, H.; Walker, C. A. Kinetics of the Hopcalite-catalyzed Oxidation of Carbon Monoxide. *AIChE J.* **1970**, *16* (2), 305–314. https://doi.org/10.1002/aic.690160226.

(8) Chout, C. L. Dynamic Modelling of Water Vapor Adsorption By Activated Alumina. *Chem. Eng. Commun.* **1987**, *56* (1–6), 211–227. https://doi.org/10.1080/00986448708911947.

(9) Nastaj, J.; Ambrożek, B. Modeling of Drying of Gases Using Solid Desiccants. *Dry. Technol.* **2009**, *27* (12), 1344–1352. https://doi.org/10.1080/07373930903383679.

(10) Ouchi, T.; Hamamoto, Y.; Mori, H.; Takata, S.; Etoh, A. Water Vapor Adsorption Equilibrium and Adsorption/Desorption Rate of Porous Alumina Film Adsorbent Synthesized with Anodization on Heat Transfer Plate. *Appl. Therm. Eng.* **2014**, *72* (2), 219–228.

https://doi.org/10.1016/j.applthermaleng.2014.05.091.

(11) Ribeiro, A. M.; Sauer, T. P.; Grande, C. A.; Moreira, R. F. P. M.; Loureiro, J. M.; Rodrigues, A. E. Adsorption Equilibrium and Kinetics of Water Vapor on Different Adsorbents. *Ind. Eng. Chem. Res.* **2008**, *47* (18), 7019–7026. https://doi.org/10.1021/ie701732x.

(12) Shi, Y. F.; Liu, X. J. Heat and Mass Transport Characteristics of Pressure Swing Adsorption for the Removal of High-Level Moisture along with CO2 from Air. *Ind. Eng. Chem. Res.* **2018**, *57* (18), 6464–6476. https://doi.org/10.1021/acs.iecr.8b00601.

(13) Brunauer, S.; Emmett, P. H.; Teller, E. Adsorption of Gases in Multimolecular Layers. *J. Am. Chem. Soc.* **1938**, *60* (2), 309–319. https://doi.org/10.1021/ja01269a023.

(14) Lastoskie, C.; Gubbins, K. E.; Quirke, N. Pore Size Distribution Analysis of Microporous Carbons: A Density Functional Theory Approach. *J. Phys. Chem.* **1993**, *97* (18), 4786–4796. https://doi.org/10.1021/j100120a035.

(15) Ursueguía, D.; Daniel, C.; Collomb, C.; Cardenas, C.; Farrusseng, D.; Díaz, E.; Ordóñez, S. Evaluation of HKUST-1 as Volatile Organic Compound Adsorbents for Respiratory Filters. *Langmuir* **2022**. https://doi.org/10.1021/ACS.LANGMUIR.2C02332.

(16) Khabzina, Y.; Farrusseng, D. Unravelling Ammonia Adsorption Mechanisms of Adsorbents in Humid Conditions. *Microporous Mesoporous Mater.* **2018**, *265*, 143–148. https://doi.org/10.1016/j.micromeso.2018.02.011.

(17) Petrazzuoli, V.; Rolland, M.; Sassanis, V.; Ngu, V.; Schuurman, Y.; Gamet, L. Numerical Prediction of Péclet Number in Small-Sized Fixed Bed Reactors of Spheres. *Chem. Eng. Sci.* **2021**, *240*, 116667. https://doi.org/10.1016/j.ces.2021.116667.

(18) Cardenas, C.; Farrusseng, D.; Daniel, C.; Aubry, R. Modeling of Equilibrium Water Vapor Adsorption Isotherms on Activated Carbon, Alumina and Hopcalite. *Fluid Phase Equilib.* **2022**, *561*, 113520. https://doi.org/10.1016/j.fluid.2022.113520.

(19) Cardenas, C. Analyse et Modélisation Du Comportement Des Caissons d'épuration de l'air Équipant Les Engins de Chantier Pour La Protection Des Opérateurs Contre Les Gaz et Vapeurs,

Université de Lorraine, 2021.

(20) Wang, L.; Liu, Z.; Li, P.; Yu, J.; Rodrigues, A. E. Experimental and Modeling Investigation on Post-Combustion Carbon Dioxide Capture Using Zeolite 13X-APG by Hybrid VTSA Process. *Chem. Eng. J.* **2012**, *197*, 151–161. https://doi.org/10.1016/j.cej.2012.05.017.

(21) Liu, Z.; Grande, C. A.; Li, P.; Yu, J.; Rodrigues, A. E. Multi-Bed Vacuum Pressure Swing Adsorption for Carbon Dioxide Capture from Flue Gas. *Sep. Purif. Technol.* **2011**, *81* (3), 307–317. https://doi.org/10.1016/j.seppur.2011.07.037.

(22) Abouelella, D. M.; Fateen, S. E. K.; Fouad, M. M. K. Multiscale Modeling Study of the Adsorption of CO2 Using Different Capture Materials. *Evergreen* **2018**, *5* (1), 43–51. https://doi.org/10.5109/1929729.

(23) Buzanowski, M. A.; Yang, R. T. Approximations for Intraparticle Diffusion Rates in Cyclic Adsorption and Desorption. *Chem. Eng. Sci.* **1991**, *46* (10), 2589–2598. https://doi.org/https://doi.org/10.1016/0009-2509(91)80052-Z.

(24) Roy, S.; Moharir, A. S. Modeling the Generic Breakthrough Curve for Adsorption Process. June 29, 2019, p 18.

(25) Cussler, E. L. *Diffusion: Mass Transfer in Fluid Systems*, Third.; Cambridge University Press: New York, 2009.

(26) Cardenas, C.; Latifi, A. M.; Vallières, C.; Marsteau, S.; Sigot, L. Analysis of an Industrial Adsorption Process Based on Ammonia Chemisorption: Modeling and Simulation. *Comput. Chem. Eng.* **2021**, *154*, 107474. https://doi.org/10.1016/j.compchemeng.2021.107474.

(27) Wakao, N.; Funazkri, T. Effect of Fluid Dispersion Coefficients on Particle-to-Fluid Mass Transfer Coefficients in Packed Beds. Correlation of Sherwood Numbers. *Chem. Eng. Sci.* **1978**, *33* (10), 1375–1384. https://doi.org/10.1016/0009-2509(78)85120-3.

(28) Rastegar, S. O.; Gu, T. Empirical Correlations for Axial Dispersion Coefficient and Peclet Number in Fixed-Bed Columns. *J. Chromatogr. A* **2017**, *1490*, 133–137. https://doi.org/10.1016/j.chroma.2017.02.026.

(29) Benesty, J.; Chen, J.; Huang, Y.; Cohen, I. Pearson Correlation Coefficient. In *Noise reduction in speech processing*; Springer, Berlin, Heidelberg, 2009; pp 1–4. https://doi.org/10.1007/978-3-642-00296-0_5.

(30) Ruthven, D. M.; Hussain, M.; Desai, R. Adsorption of Water Vapor on Activated Alumina. *Stud. Surf. Sci. Catal.* **1993**, *80* (C), 545–552. https://doi.org/10.1016/S0167-2991(08)63559-4.

(31) Liu, X. J.; Shi, Y. F.; Kalbassi, M. A.; Underwood, R.; Liu, Y. S. A Comprehensive Description of Water Vapor Equilibriums on Alumina F-200: Adsorption, Desorption, and H2O/CO2 Binary Adsorption. *Sep. Purif. Technol.* **2014**, *133*, 276–281. https://doi.org/10.1016/j.seppur.2014.06.052.

(32) Ahn, H.; Lee, C. H. Adsorption Dynamics of Water in Layered Bed for Air-Drying TSA Process. *AIChE J.* **2003**, *49* (6), 1601–1609. https://doi.org/10.1002/aic.690490623.

(33) Ahn, H.; Lee, C. H. Effects of Capillary Condensation on Adsorption and Thermal Desorption Dynamics of Water in Zeolite 13X and Layered Beds. *Chem. Eng. Sci.* **2004**, *59* (13), 2727–2743. https://doi.org/10.1016/j.ces.2004.04.011.

(34) Ahn, H. Equilibrium Theory Analysis of Thermal Regeneration of a Humid Adsorption Column: Selection of Optimal Hot Purge Gas Temperature. *Chem. Eng. Res. Des.* **2019**, *151*, 91–99. https://doi.org/10.1016/j.cherd.2019.08.018.

(35) Athalye, A. M.; Gibbs, S. J.; Lightfoot, E. N. Predictability of Chromatographic Protein Separations. Study of Size-Exclusion Media with Narrow Particle Size Distributions. *J. Chromatogr. A* **1992**, *589* (1–2), 71–85. https://doi.org/10.1016/0021-9673(92)80007-H.

(36) Delgado, J. M. P. Q. A Critical Review of Dispersion in Packed Beds. *Heat Mass Transf.* **2006**, *42* (4), 279–310. https://doi.org/10.1007/s00231-005-0019-0.

(37) Valdés-Solís, T.; Linders, M. J. G.; Kapteijn, F.; Marbán, G.; Fuertes, A. B. Adsorption and Breakthrough Performance of Carbon-Coated Ceramic Monoliths at Low Concentration of n-Butane. *Chem. Eng. Sci.* **2004**, *59* (13), 2791–2800. https://doi.org/10.1016/j.ces.2004.03.025.

(38) Knox, J. C.; Ebner, A. D.; Levan, M. D.; Coker, R. F.; Ritter, J. A. Limitations of Breakthrough

Curve Analysis in Fixed-Bed Adsorption. *Ind. Eng. Chem. Res.* **2016**, *55* (16), 4734–4748. https://doi.org/10.1021/acs.iecr.6b00516.

(39) Esposito, F.; Cardenas, C.; Latifi, A. M.; Marsteau, S. CFD Modeling and Simulation of an Ammonia Adsorption Process. In *32nd European Symposium on Computer Aided Process Engineering*; Montastruc, L., Negny, S., Eds.; Elsevier, 2022; Vol. 51, pp 463–468. https://doi.org/10.1016/B978-0-323-95879-0.50078-3.

(40) Ruthven, D. M.; Farooq, K.; Knaebel, K. S. *Pressure Swing Adsorption*; VCH: New York, 1994.

(41) Sun, T.; Seff, K. Silver Clusters and Chemistry in Zeolites. *Chem. Rev.* **1994**, *94* (4), 857–870. https://doi.org/10.1021/cr00028a001.

(42) Cardenas, C.; Sigot, L.; Vallières, C.; Marsteau, S.; Marchal, M.; Latifi, A. M. Ammonia Capture by Adsorption on Doped and Undoped Activated Carbon: Isotherm and Breakthrough Curve Measurements. *Sep. Purif. Technol.* **2023**, *313*, 123454. https://doi.org/10.1016/J.SEPPUR.2023.123454.

(43) Cardenas, C.; M. Latifi, A.; Vallières, C.; Marsteau, S. Analysis of an Industrial Adsorption Process Based on Ammonia Chemisorption: Model Validation. In *32nd European Symposium on Computer Aided Process Engineering*; Montastruc, L., Negny, S., Eds.; Elsevier, 2022; Vol. 51, pp 457–462. https://doi.org/10.1016/B978-0-323-95879-0.50077-1.

(44) Willmott, C. J. On the Validation of Models. *Phys. Geogr.* **1981**, *2* (2), 184–194. https://doi.org/10.1080/02723646.1981.10642213.

(45) Chowdhury, S.; Saha, P. Das. Comparative Analysis of Linear and Nonlinear Methods of Estimating the Pseudo-Second-Order Kinetic Parameters for Sorption of Malachite Green onto Pretreated Rice Husk. *Bioremediat. J.* **2011**, *15* (4), 181–188. https://doi.org/10.1080/10889868.2011.624140.

(46) Cardenas, C.; Latifi, A. M.; Vallières, C.; Marsteau, S. Multiscale Modeling of Ammonia Adsorption on Zinc Sulfate-Doped Activated Carbon: Sensitivity Analysis, Parameter Identification, and Model Validation. *Sep. Purif. Technol.* **2023**, *322*, 124173.

https://doi.org/10.1016/j.seppur.2023.124173.

Graphic for Manuscript